



Solar-activated tandem thin films based on CuInS_2 , TiO_2 and SnO_2 in optimized wastewater treatment processes

Alexandru Enesca^{a,*}, Mazabalo Baneto^b, Dana Perniu^a, Luminita Isac^a, Cristina Bogatu^a, Anca Duta^{a,*}

^a Center for Renewable Energy System and Recycling, R&D Institute of the Transilvania University of Brasov, Eroilor 29 Street, 500036 Brasov, Romania

^b CUER-UL, Lomé Univeristy, BP: 1515, Lomé, Togo

ARTICLE INFO

Article history:

Received 30 July 2015

Received in revised form

24 December 2015

Accepted 31 December 2015

Available online 6 January 2016

Keywords:

Tandem semiconductors

CIS

Band gap

Interface control

Photocatalysis

ABSTRACT

Tandem structures involving CuInS_2 , TiO_2 and SnO_2 thin films were prepared by Robotic spray pyrolysis and were optimized in terms of composition and deposition temperatures. The compounds have structural compatibility (crystalline structures and crystallites sizes) and good homogeneity. The crystalline structures were investigated by X-ray diffraction and the morphology by atomic force microscopy and scanning electron microscopy. The wettability properties and the surface energy were calculated based on contact angle measurements using two liquids with different polarities (glycerol and ethylene glycol). The components in the tandem systems have suitably positioned the energy of the conduction and valance bands, limiting charge recombination, therefore, the sample containing all three semiconductors has the highest mineralization efficiency (95.3% removal of total organic carbon) under UV + Vis irradiation, mimicking solar radiation. Long term use of the photocatalytic films (up to 36 h) proved the need to design the process with interim washing steps for preserving the photocatalytic efficiency by avoiding surface clogging.

© 2016 Elsevier B.V. All rights reserved.

1. Introduction

Advanced oxidation processes (AOPs) have emerged as a promising alternative route to traditional processes such as adsorption, bioremediation, and coagulation/flocculation. The main advantage of AOPs is their capability to rapidly degrade a wide range of recalcitrant pollutants in the aquatic environment [1–3], even at low concentrations. Such effective remediation of aquatic hazardous substances is attributed to the in situ generation of hydroxyl radicals ($\cdot\text{OH}$) as primary transient oxidant species, [4–6]. Identifying novel photocatalytic materials suitable for AOPs is a continuous challenge due to the specific properties that are required: chemical stability in the working environment, activation under solar (UV–vis) irradiation, high concentration of charge carriers, lack of toxicity and cost effectiveness [7,8].

Many studies report on the photocatalytic activity of metal oxides such as TiO_2 [9], WO_3 [10], ZnO [11], SnO_2 [12], and their combinations in composite materials. The papers discussing hybrid materials or simple tandem system identified mainly two

limitations with effect on the photocatalytic efficiency: the position of the energy bands and the low chemical stability [13–15]. Promising tandem systems with (almost) suitable energy bands alignment are mentioned as ZnO/TiO_2 [16], WO_3/TiO_2 [17], $\text{SnO}_2/\text{TiO}_2$ [18], mostly active in UV, or $\text{Cu}_x\text{S}/\text{TiO}_2$ [19], and $\text{ZnO}/\text{Cu}_2\text{O}$ [20], that are stable only in a limited pH range; this shows that finding UV–vis active, aqueous-stable materials with suitable position of the energy levels is still a problem that has to be addressed.

The main objective of this paper is to propose a novel group of photocatalytic tandem systems able to support advanced oxidations processes (AOPs) under solar radiation (UV and Vis irradiation). The concept is based on the photovoltaic cell properties in which the materials (CIS, TiO_2 and SnO_2) and their position in the final structure where chosen in order to fulfill two objectives: (1) the effective band gap value allows high UV–vis absorption with high mobility of the charge carriers and (2) chemical stability in the working environment for long periods (36 h). Using multi-component structures in photocatalytic processes, charge recombination can be reduced and the charge carrier's number is expected to increase, being further involved in the formation of oxidative species. These systems were obtained by robotic spray pyrolysis deposition (RSPD) and annealed to improve crystallinity. The tandems were designed based on the position of

* Corresponding authors.

E-mail addresses: aenesca@unitbv.ro (A. Enesca), a.duta@unitbv.ro (A. Duta).

the conduction and valence bands of each component, and were selected also considering the chemical stability and crystalline structure compatibility. The photocatalytic activity was tested in aqueous solution to demonstrate the efficiency and durability of these tandem systems in mineralization processes. Considering the possibility of up-scaling for industrial applications, the long term stability of the samples was tested and intermediate washing steps were demonstrated to preserve the photocatalytic long-term efficiency by avoiding surface loading with the pollutant or the photodegradation by-products.

2. Experimental procedure

2.1. Precursor preparation and deposition parameters

Robotic spray pyrolysis deposition (RSPD) was employed to prepare seven types of samples containing SnO_2 , TiO_2 and CuInS_2 . The substrate was $2\text{ cm} \times 2\text{ cm}$ microscopic glass (Heinz Herenz) cleaned by successive immersion in ethanol and acetone, using an ultrasonic bath.

The precursor for SnO_2 films was prepared by mixing tin chloride (SnCl_4 , 99.99%, Alfa Aesar) with ethanol ($\text{C}_2\text{H}_5\text{OH}$, 99.99%, Alfa Aesar) to form 0.1 M solutions. The precursor for TiO_2 films was prepared by mixing titanium chloride (TiCl_4 , 99.99%, Alfa Aesar) with ethanol ($\text{C}_2\text{H}_5\text{OH}$, 99.99%, Alfa Aesar) to form 0.05 M solutions. Finally, the CuInS_2 films were prepared from 0.3 M copper chloride (CuCl_2 , 99%, Scharlau), 0.3 M indium chloride (InCl_3 , 99.5%, Scharlau) and thiourea ($\text{SC}(\text{NH}_2)_2$, 99%, Scharlau) in a 1:1.25:4.5 molar ratio.

The depositions parameters were selected based on previous studies [21,22] which showed that the use of inorganic precursors leads to fast nucleation and increases the film uniformity, having also the advantage of lower toxicity and costs, as compared to the organic–metallic precursors. The number of spraying sequences was set at 20 for each component layer but the break between two pulses was optimized at: 45 s for tin oxide, 60 s for titanium oxide and 30 s for copper compounds. The carrier gas was compressed air and the deposition pressure was 1.4 bar in all experiments. Details on the samples deposition are synthesized in Table 1.

To improve crystallinity, deposition was followed by annealing at 300°C , for 5 h.

2.2. Photocatalysis in aqueous solution

The photodegradation reactor consists of a static cylindrical flask, open to air.

Combined UV and Vis radiation was employed during the photocatalytic experiments by using one F18W/T8 (black light tube, UVA, typically 340–400 nm, with $\lambda_{\text{max}} = 365\text{ nm}$, flux intensity $3\text{ L}\times$, Philips) and two TL-D Super 80 18W/865 lamps (white cold light tubes, Vis, typically 400–700 nm, with $\lambda_{\text{max}} = 565\text{ nm}$, flux intensity $28\text{ L}\times$, Philips), placed annular to the photoreactor. This combination was chosen as it mimics the solar spectrum (excluding the IR part).

The pollutant tested in this work was 0.0125 mM methylene blue (99.8%, Merck) prepared by dissolving the powder in ultra pure water (Direct-Q3 Water Purification System). Methylene blue photocatalytic mineralization was evaluated using a Total Organic Carbon and Total Nitrogen Analyzer (TOC-L+TNM-L, Shimadzu model TOC-LCPH). Experiments used the auto-sample mode at 1 h interval during 6 h. Photocatalytic removal efficiency of MB was estimated based on UV–vis spectra (PerkinElmer Lambda 950 UV–Vis–NIR), based on the calibration curve at $\lambda_{\text{max,MB}} = 665\text{ nm}$.

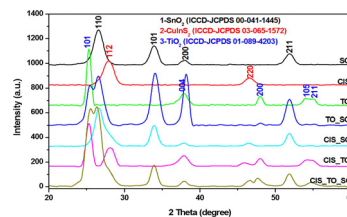


Fig. 1. XRD patterns of individual and tandem layers.

Before irradiation, each thin film sample ($2\text{ cm} \times 2\text{ cm}$) was inserted in a quartz beaker, in 25 mL dye solution and was kept in dark for 2 h to reach the adsorption equilibrium.

The long term stability tests were conducted in three cycles of 12 h each. At the beginning of each cycle the methylene blue solution was replaced with a fresh one having the same initial concentration (0.0125 mM) in order to simulate an intensive industrial application.

All experiments were done in static regime, without stirring; this was considered the worst case scenario (diffusional control only), and is close to the up-scaled operation regime, when the polluted water passes over the film in a laminar flow.

2.3. Thin films characterization

The crystalline structure and composition of the annealed layers were evaluated by X-Ray Diffraction (XRD, Bruker D8 Discover Diffractometer) using the locked-couple technique with 0.002° scan step and 0.01 s/step . The surface morphology of the individual and tandem layers was investigated using an Atomic Force Microscope (AFM, NT-MDT model BL222RNTE), with images taken in semicontact mode with Si-tips (NSG10, force constant 0.15 N/m , tip radius 10 nm); complementary scanning electron microscopy (SEM, Hitachi model S-3400 N type 121 II) was employed. The specific/BET surface was evaluated based on the nitrogen adsorption isotherms measured at 77 K (Autosorb IQ-MP, Quantachrome analyzer). The substrate (microscopic glass) and thin films (with similar surface and weight) were initially degassed for 3 h at 250°C . The BET specific surface of uncoated glass was very low ($0.002\text{ m}^2/\text{g}$), thus the contribution of the glass substrate in the as-measured specific surface was neglected.

Static contact angle measurements with the sessile drop method were recorded and analyzed using an OCA-20Contact Angle-meter (DataPhysics Instruments). Energy dispersive X-ray spectroscopy (Ultra Dry, Noran System 7, NSS Model) was used to identify the energy values corresponding to each element on the samples surface.

3. Results and discussions

3.1. Crystalline structure and morphology

The development of compatible crystalline structures between the compounds in the tandem systems is confirmed by the diffraction data in Fig. 1.

The mechanism of film formation includes: nucleation, development of the incipient layer and formation of the bulk structure based on aggregates growth and sintering. Previous work showed that the use of inorganic precursors leads to fast nucleation and increases the film uniformity [23]. The optimized break between pulses allows the solid-state reactions to complete and avoids undesired by-products trapped in the films. The crystallization process is supported by two factors: (1) optimal (and high) deposition temperature and (2) similarity in the crystalline structures at the interfaces between the components in the tandem. Therefore, the

Table 1
Individual and tandem structures obtained by RSPD.

Sample abbreviation	Sample structure	Precursors and deposition temperature for each layer		
		1st Layer	2nd layer	3rd layer
SO	SnO ₂	SnO ₂ : SnCl ₄ , C ₂ H ₅ OH; 400	–	–
CIS	CuInS ₂	CuInS ₂ : CuCl ₂ , InCl ₃ , SC(NH ₂) ₂ , H ₂ O:C ₂ H ₅ OH; 300	–	–
TO	TiO ₂	TiO ₂ : TiCl ₄ , C ₂ H ₅ OH; 450	–	–
TO.SO ^a	TiO ₂ /SnO ₂	SnO ₂	TiO ₂	–
CIS.TO ^a	CuInS ₂ /TiO ₂	TiO ₂	CuInS ₂	–
CIS.SO ^a	CuInS ₂ /SnO ₂	SnO ₂	CuInS ₂	–
CIS.TO.SO ^a	TiO ₂ /SnO ₂ /CuInS ₂	SnO ₂	TiO ₂	CuInS ₂

^aEach component in the multi-layered structure was obtained in identical conditions as the correspondent single-layer sample.

deposition and annealing temperatures were optimized to get a high crystallinity degree (a pre-requisite in opto-electronic applications), and compatible individual crystalline structures, able to develop continuous interfaces that support charge carriers mobility through the tandem structure, thus limiting recombination, [24].

The formation of thin films with similar crystallite sizes (see Table 2) and crystallization systems indicates interfacial lattice compatibility, starting with the early stages of the deposition processes.

Using the Scherrer's formula the crystallite sizes were evaluated and the micro-strains were calculated using the Bruker EVA software based on the diffraction spectra. The crystallite sizes (and in some extent their aggregates size) are directly influenced by the ratio of the nucleation and crystal growth rates, and by their individual values, [25].

The metal oxides form small crystallites with comparable size and have two compatible crystallization plans (101 and 200). The deposition of a second and third layer on TiO₂ and SnO₂ has little influence on their crystallite sizes (less than 5%); the slight fluctuation can be correlated with the longer residence time on the heated plate, which allows reorganization during the predominant growth process; however, this effect also depends on the top-layer density, thus explaining the slight variation in the SnO₂ and TiO₂ in the two- and three layered structures. The micro-strain values in Table 2 are small and confirm the lattice match in the oxide mono- and multi-layers.

The size of the CuInS₂ crystallites significantly decreases (~12%) when deposited on the metal oxides (with significantly higher roughness than glass), proving a faster nucleation, governed by the high energy points on the oxides with a rather large ionic degree. However, it is to notice that the micro-strain values in the CIS mono-layer are higher than the corresponding values in the multi-layers, as crystal growth occurs in an environment with a higher expansion of thermal energy which explains why longer resident time (CIS.TO.SO sample) on the heating plate induces a network relaxation and reduces the micro-strains.

The crystallite sizes were further correlated with the roughness values obtained from the AFM analyses (Fig. 2). Roughness may originated following random crystallites growth and/or crystallites association in aggregates. The ratio between the aggregate sizes (evaluated by Fourier transformation of AFM/3D topography measured in semi-contact mode) and the crystallites' size (calculated based on the XRD data) allows estimating the average number of crystallites in the aggregates.

As the data in Table 2 show, the multi-layers have a higher roughness than the individual mono-layers; however, the number of crystallites forming aggregates is almost constant in the oxide layers, thus the roughness difference between the TiO₂ as mono-layer (TO sample) and as second-layer (TO.SO sample) is the results of a more random growth and not of agglomeration.

There is a larger roughness increase in the structures having CIS as outer layer and this can be the result of two combined factors:

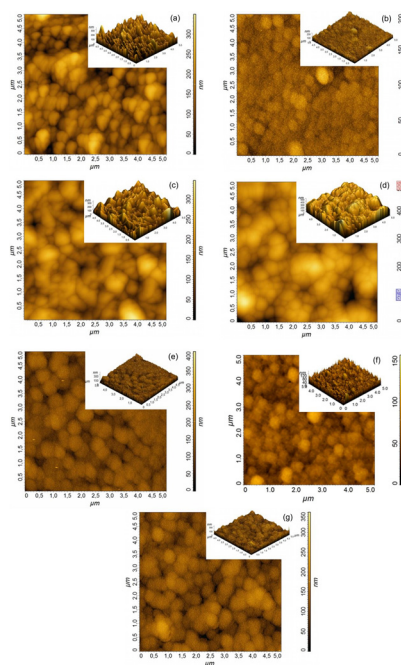


Fig. 2. AFM 2D and 3D images of: (a) SO, (b) CIS, (c) TO, (d) TO.SO, (e) CIS.SO, (f) CIS.TO and (g) CIS.TO.SO.

(a) the crystallite size of the substrate layer and its compatibility with the next deposited one, as the samples containing larger crystallite sizes (~80 Å) have a smoother surface than the samples with smaller crystallites (~70 Å), proving the faster nucleation and less ordered growth [26,27]; (b) aggregation of CIS crystallites, as the average number of crystallites increases from the CIS mono-layer (24 crystallites) to the CIS as top layer (28 crystallites). Thus, there is a competition between nucleation, growth and aggregation, governed by the crystallographic match. Previous investigations [21], showed that irregular interpenetration of the successive layers (following these mechanisms) have as result the roughness increase. Thin layers as the tandem structures hereby reported, have rather low roughness variations for multi-layers with similar chemical composition (e.g., layers CIS, with roughness variations lower than 5 nm) outlining that, the chemical composition mainly influences this process.

Additionally, the deposition temperature allows the kinetic control during the growth mechanisms: the TiO₂ layers obtained at higher temperature (450 °C) are more compact (average of 60 crystallites per aggregate). Thus, by corroborating the precursor composition and the deposition parameters the interface and surface control is possible in the tandem systems.

Overall, the AFM analyses (Fig. 2) show the formation of dense granular morphologies with a random growth for metal oxides.

Table 2
Crystallinity data and surface properties of the samples.

Samples code	Crystallite size [Å]			Average number of crystallites in the aggregates			Crystallization system/micro-strain (ε)			Roughness [nm]	S _{BET} [m ² /g]
	SnO ₂	TiO ₂	CuInS ₂	SnO ₂	TiO ₂	CuInS ₂	SnO ₂	TiO ₂	CuInS ₂		
SO	82.0	–	–	30.5	–	–	TRG ^a /0.027	–	–	27.5	0.017
CIS	–	–	82.8	–	–	24.0	–	–	BCT ^b /0.051	33.6	1.017
TO	–	81.6	–	–	61.0	–	–	TRG/0.025	–	34.6	0.034
TO.SO	83.1	85.5	–	30.0	58.5	–	TRG/0.030	TRG/0.032	–	37.5	0.538
CIS.SO	84.1	–	71.3	30.0	–	28.0	TRG/0.033	–	BCT/0.043	40.7	1.548
CIS.TO	–	83.2	72.6	–	60.0	27.5	–	TRG/0.028	BCT/0.045	43.7	1.260
CIS.TO.SO	82.3	81.4	71.5	30.0	61.5	28.0	TRG/0.027	TRG/0.025	BCT/0.043	45.5	1.320

^aTRG: tetragonal; ^bBCT: body centered tetragonal.

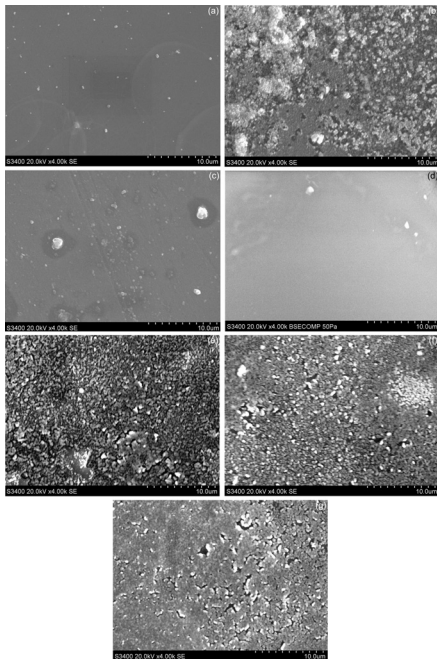


Fig. 3. SEM picture of: (a) SO, (b) CIS, (c) TO, (d) TO.SO, (e) CIS.SO, (f) CIS.TO and (g) CIS.TO.SO.

Regular growth giving strawberry-like structure was observed in the case of lower crystallite sizes (CuInS₂) [28,29].

In terms of uniformity, the samples with TiO₂ top layer (TO and TO.SO) contain grains with various sizes (100–700 nm) randomly distributed on the surface. The formation of large uniform structures and dense morphologies is a consequence of small aggregates sintering. Contrary, when SnO₂ and CuInS₂ are the top layers, the surface is homogenous with grains up to 300 nm.

The roughness values are important in the photocatalytic applications which are interface dependent processes, positively influenced by: (1) large specific surfaces with high amount of active sites, and (2) light multi-scattering processes, [30,31] ; on the other hand, too high roughness can support mechanical surface damage along with local dissolution and leaching.

The SEM analysis (Fig. 3) was done at high vacuum without metallic coverage. The samples with SnO₂ (Fig. 3a) and TiO₂ (Fig. 3c and d) as top layer show residual powder on the top, formed during the deposition when the temperature above the substrate is high enough to induce complete solvent evaporation and reaction in the smallest aerosol droplets. When CuInS₂ is the top layer (Fig. 3b, e–g), various surface defects can be observed (cracks and holes) due to the fast precursor evaporation. When CuInS₂ is deposited onto TiO₂ the amount of these defects is decreasing but the cracks are larger (Fig. 3e and g) as a possible consequence of the

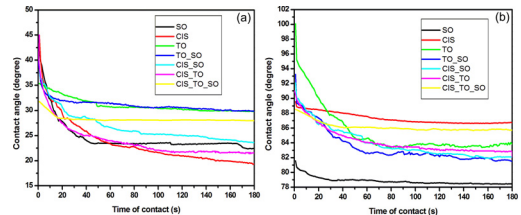


Fig. 4. Contact angle measurements with (a) glycerol and (b) ethylene glycol.

different aggregation. These results show that besides crystallinity, aggregation by sintering must also be considered when discussing the layers' and interfaces compatibility.

The specific surface is an important property in any catalytic process, including photocatalysis. As expected for thin, rather dense films, the BET specific surface values (Table 2) are low; however significant differences occur and these are not identically following the roughness variation (e.g., the micro- and nano-pores governing the specific surface values are in a lower amount in the oxide samples than in the CIS layer, although the CIS and TO samples have a similar roughness). The strawberry-like CIS structure in mono- and multi-layered samples is responsible for much larger specific surfaces and a potentially higher amount of active sites on the crystalline edges and corners. A significant increase in the specific surfaces is observed for the tandem layers, comparing to the mono-layers, confirming the growth/aggregation competition, down to the nano-pores level.

Wetting is important because the pollutants and water adsorption represents the first step in an efficient photocatalytic process. The surface energy was therefore evaluated based on contact angle measurements (Fig. 4). The contact angle mainly depends on the surface chemical composition, morphology/topology, and density

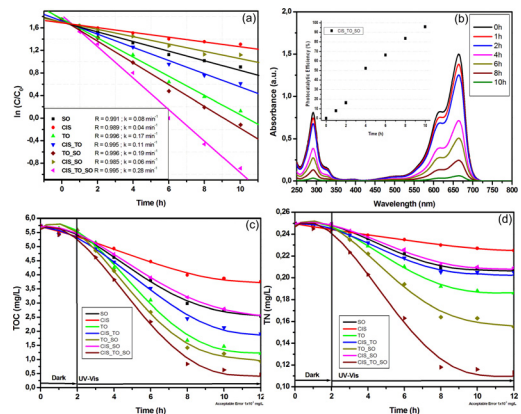


Fig. 5. Photocatalytic activity of the tandem systems: (a) first-order decay curve, (b) UV–vis spectra during MB degradation on CIS.TO.SO (inset: MB bleaching efficiency), (c) total organic carbon (TOC) and (d) total nitrogen (TN).

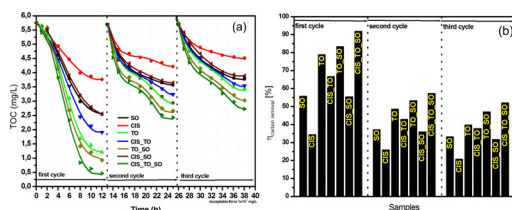


Fig. 6. TOC evolution for long time photocatalytic experiments (a) mg/L and (b) percentage.

[32,33]. Recent experimental studies show that textured surfaces, with roughness lower than 100 nm, are mainly changing the shape of the water droplet on the surface and less the contact angle value [34].

Water contact angles were measured and showed a hydrophilic behavior for all the samples, Table 3, with values of 10–15°. The lowest contact angles correspond to the samples having CIS as outer layer, proving that the surface roughness and homogeneity are more important than the ionic degree. These low contact angles also allow a very short time for reaching surface wetting equilibrium, which represents an advantage in photocatalysis.

To outline the influence of the surface chemistry, two liquids with much lower polarity and higher viscosity than water were used: glycerol (with the polar component of the surface energy $\sigma^p = 41.50$ mN/m and the dispersive component of $\sigma^d = 21.20$ mN/m) and ethyleneglycol (with the polar component $\sigma^p = 19$ mN/m and the dispersive component $\sigma^d = 29$ mN/m). The contact angle values and their evolution over 180 s are presented in Fig. 4. As expected, the more polar glycerol supports lower contact angle values, proving that surface interactions are governed also by chemistry. The small fluctuation after equilibrium is reached, prove that there is a certain heterogeneity in the surface topology, but this is low. The results also show that the cracks formed on the surface of the samples with CIS top layer are superficial, not affecting the depth of the film, as the contact angles have a slow decrease until reaching equilibrium.

The experimental surface energy was calculated according to Eq. (1), [35]:

$$\sigma_{LV}(1 + \cos \theta) = 2 \left[(\sigma_{LV}^p \sigma_{SV}^p)^{1/2} + (\sigma_{LV}^d \sigma_{SV}^d)^{1/2} \right] \quad (1)$$

where: σ_{LV}^p , σ_{SV}^p , σ_{LV}^d , σ_{SV}^d are the apparent polar and dispersive components of the liquid- and solid- surface energies, respectively

As the results in Table 3 show, the samples containing metal oxides have an experimental surface energy dominated by the apparent polar component indicating good wettability; this is particularly obvious after reaching the wetting equilibrium, i.e., 40–60 s (Fig. 4), and makes them suitable candidates for applications in aqueous solutions and humid media.

By comparing the experimental surface energy and the roughness values it can be noticed that values lower than 100 mN/m correspond to the samples containing metal oxide as top layer and values larger than 100 mN/m correspond to samples having CIS as top layer. Consequently the measurements indicate that the contact angle of low polarity liquids can better outline the influence of the chemical composition on the overall surface energy (affecting the absorption behavior) [36].

3.2. Photocatalysis in aqueous solution

The photocatalytic activity was tested in aqueous solution using methylene blue (MB) as reference pollutant. The decrease in the MB concentration (Fig. 5a and b) was evaluated based on the UV–Vis calibration curve and the photocatalytic activity toward mineral-

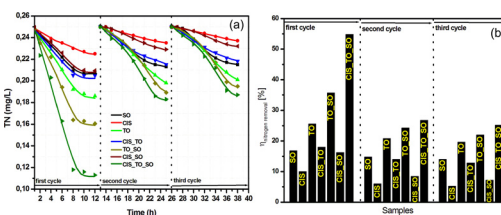
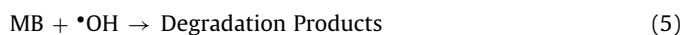


Fig. 7. TN evolution for long time photocatalytic experiments (a) mg/L and (b) percentage.

ization was investigated by using TOC (Fig. 5b) and TN (Fig. 5c) measurements.

The results show that adsorption (in dark) is rather slow (Eq. (2)) and could be the limiting step in the photocatalytic mechanism, while the contribution of cumulative charge generation through the tandem structure will facilitate the formation of oxidative species which will increase the efficiency of the mineralization mechanism (Eqs. (3)–(5)):



As expected, the pseudo-first order well describes the MB removal process (Fig. 5a). The highest MB bleaching efficiency corresponds to an *n*–*n* tandem, $\text{TiO}_2/\text{SnO}_2$ (86.8%), and to the *p*–*n*–*n* structure, $\text{CuInS}_2/\text{TiO}_2/\text{SnO}_2$ (95.9%). The contribution of CuInS_2 in the $\text{TiO}_2/\text{SnO}_2$ tandem structure is significant, also considering that $\text{CuInS}_2/\text{TiO}_2$ and $\text{CuInS}_2/\text{SnO}_2$ support much lower efficiencies (68.7% and 57.4%).

The UV–Vis spectra for the most representative sample (CIS_TO_SO) obtained during the whole MB degradation process (Fig. 5b) shows that there are no extra-peak or displacement of the peaks maxima during the photocatalytic processes, thus there is no UV–Vis sensitive by-product formed during the process. Additionally, the differences in kinetics are mirrored in the efficiency curve, with a change in the slope between adsorption in dark and photocatalysis under irradiation (after two hours in dark).

According to the TOC measurements, the highest photocatalytic activity was observed for the sample CIS_TO_SO which shows after 12 h of UV + Vis irradiation a total organic carbon removal of 92.3% (Fig. 5b) and 52% of the total nitrogen (Fig. 5c). These values confirm that adsorption, photo-bleaching and mineralization occur at different rates (particularly for nitrogen removal, with higher pollution potential). The results also show that if water re-use is the final target, monitoring the photocatalytic process only based on the bleaching efficiency and TOC decrease might not be enough, and additional treatment is required to remove the nitrogen-containing compounds.

The robotic spray pyrolysis deposition is an easily up-scalable technique, able to be implemented as an industrial technology, thus these photocatalytic thin layers could represent a viable option for

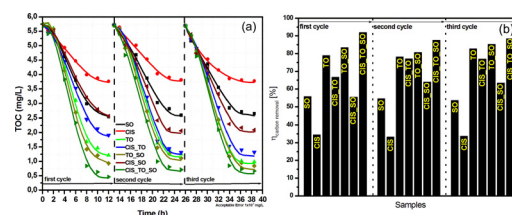


Fig. 8. TOC evolution for long time photocatalytic experiments with cleaning step after each cycle (a) mg/L and (b) percentage.

Table 3
Water contact angles and experimental surface energy of the thin films.

Sample abbreviation	θ_{Water} [degree]	Total surface energy σ [mN/m]	Dispersive component of the surface energy σ_d [mN/m]	Polar component of the surface energy σ_p [mN/m]
SO	14.3	92.35	30.62	61.73
CIS	10.4	138.36	64.84	73.52
TO	13.9	81.95	28.71	53.24
CIS.SO	11.6	115.73	49.36	66.37
CIS.TO	11.2	108.44	32.25	76.19
TO.SO	14.1	72.85	22.34	50.51
CIS.TO.SO	11.1	124.09	58.35	65.74

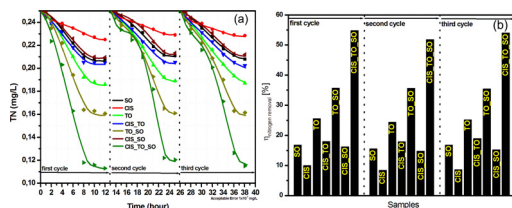


Fig. 9. TN evolution for long time photocatalytic experiments with cleaning step after each cycle (a) mg/L and (b) percentage.

further advanced wastewater treatment; therefore, their long-term stability under static operating conditions was tested.

The samples were immersed in MB 0.0125 mM solution for an overall duration of 36 h (3 cycles of 12 h each). At the end of each cycle the pollutant solution was replaced with a fresh one having the same concentration (0.0125 mM) and without further intervention on the photocatalyst films. The TOC (Fig. 6) and TN (Fig. 7) evolution was observed.

An interesting finding is the significant decay in the photocatalytic efficiency, starting with the second cycle; another observation is that the organic carbon and nitrogen removal reach almost similar saturation levels during the second and third cycles. The reduction of the photocatalytic properties represent a severe problem when integration in industrial applications is expected. Two main (and different) reasons could explain this behavior: (1) photocatalyst load with by-products or (2) irreversible degradation of the photocatalytic layer due to photo-corrosion, wash-out, etc. To elucidate this behavior a new set of experiments was done, under similar conditions but with an interim step of cleaning the photocatalyst films by immersion in water after each cycle, for 10 s. The TOC and TN evolution can be observed in Figs. 8 and 9.

Under these experimental conditions the photocatalytic properties and the mineralization efficiencies remain high even after three cycles. The results confirm that the catalytic surface accumulates during the photocatalytic process different by-products, including adsorbed gases resulted in mineralization. However, a simple water cleaning procedure can re-activate the interface allowing high efficient removal of organic pollutants (up to 92% for CIS.TO.SO); in an up-scaled version of this process, a short water back-current step, at optimized time intervals, can regenerate the substrate. In the experimental design, this step is recommended after 8–9 h, before equilibration/saturation is reached.

The evolution of nitrogen removal is lower compared with that of total organic carbon, which indicates the persistence of nitrogen compounds. It was observed that the CIS.SO sample increases the photocatalytic activity with 10% after the second cycle, as result of a possible conditioning step. However, the TOC and TN values after the first 12 h cycle are very close to those obtained after 6 h of UV + Vis irradiation, proving that nitrogen advanced removal cannot be improved by increasing the photocatalytic duration in the experimental conditions. Future work will be dedicated to optimizing this issue.

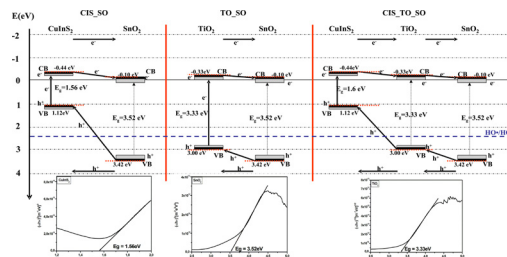


Fig. 10. Energy levels diagram for the tandem structures (inset: Eg values and EDX spectra).

Table 4
Effective band gap of the tandem systems.

Sample	TO.SO	CIS.TO	CIS.(TO).SO
Effective band gap [eV]	3.0	1.45	1.22

The pollutant removal and mineralization efficiencies are usually enhanced by large specific surfaces of the photocatalyst; this is valid for powder photocatalysts, with large specific surfaces but is less important for thin films, which actually have much lower BET surfaces. One example is the CIS mono-layer with the lowest TOC and TN removal efficiencies but with the BET surface of 1–1.5 m²/g, larger than any other oxide mono- or bi-layer. Thus, the charge carriers generation and recombination can be identified as the most important processes in the thin-film based processes.

Modelling the band structures (Fig. 10) allows understanding the experimental results. The charge carriers injection and mobility fundamentally depend on the values of the energy bands, and were calculated according to the algorithms presented by Mise and Nakada [37], and Gao [38]. The method for evaluating the valence band (VB) and conduction band (CB) potentials for semiconductors was previously presented [39].

The effective band gap of the tandem systems was calculated according to Scanlon et al. [40] and the values are presented in Table 4, confirming the extended Vis activation of the structures that contain CuInS₂, but also lower activation energies in the metal-oxide two-layer films, as compared to the mono-layers. Thus, the difference in the mineralization efficiencies in these tandems should mainly rely on the ability to support charge separation.

According to the bands energy diagram, the electrons from the tin oxide valence band are promoted on: (1) titanium oxide valence band which is the closest energy, in the TO.SO sample; (2) copper indium disulfide valence band, in the case of CIS.SO sample and (3) titanium oxide valence band, which acts as transitory energy level to copper indium di-sulfide valence band, in the CIS.TO.SO sample.

Under light irradiation, electron-hole pairs are generated [41,42]; at the *n-p* interface/junction the pairs generated within the charged space region can be more effectively separated by the electric field. The *n-n* interface (between metal oxides) and *n-p* junctions (between CuInS₂ and metal oxides) have similar effects

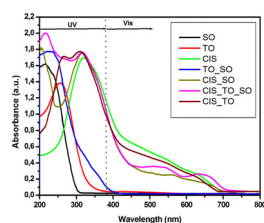


Fig. 11. Absorbance spectra of mono-component and tandem structures.

in both photovoltaic and photocatalytic applications, i.e., the transfer of the charge carrier involved in the process. As mentioned in literature [43,44] the shift in the band gaps is quite low in the case of metal oxides junctions if the stoichiometry is preserved (which is likely in this case).

The injection of new charge carriers in the depletion layer will increase the concentration gradient over the semiconductor, resulting in the formation of a diffuse layer, [45,46]. Therefore, a current will flow due to a combined effect of drift and diffusion by photo-generated electrons. The conduction band (CB) edges of SnO_2 and TiO_2 are conveniently located at -0.10 and -0.33 eV vs. normal hydrogen electrode (NHE). The valence band (VB) edge of SnO_2 ($+3.42$ eV) is lower than that of TiO_2 ($+3.00$ eV). In the case of CIS_TO_SO sample the charge carrier's diffusion continuously evolve form the TiO_2 valence band to the CuInS_2 valence band which is located at $+1.12$ eV. Thus, charge recombination is significantly reduced in the tandem films, as compared to single films, allowing a faster electron-transfer process from the conduction band of CuInS_2 to that of TiO_2 and SnO_2 , which will support the formation of holes and further on, of oxidative species during the photocatalytic removal organic pollutants from wastewater, [47,48].

As Fig. 10 shows, the reaction of holes with water, Eq. (4) forming the hydroxyl radical is supported by the oxidation potential (2.40 eV) when the photocatalysts are CIS_TO_SO, SO_TO and CIS_SO. On the other hand, the differences between these substrates in TOC and TN removal can be related to the faster recombination in CIS_SO, which is the consequence of the rather larger difference in the VB values.

The mineralization process mostly depends on the photocatalyst ability to produce and convert a high amount of charge carriers into oxidative species without significant surface corrosion [49,50]. The stability to photo-corrosion was proved by the three-cycle experiments, and the $\text{CuInS}_2/\text{TiO}_2/\text{SnO}_2$ tandem system insures an extended and continuous charge carriers' flow, which uses both UV and Vis radiation, thus this type of system fulfills both prerequisites. This is also confirmed by the much faster MB removal, with a rate constant 1.5 times higher than TiO_2 , thus a larger amount of oxidative species.

The data also show that the mineralization mechanism is complex (but quite similar for all the photocatalytic substrates), and involves two major sequences: in the first 6–8 hours there is a fast decomposition toward mineralization of the most active C and N-containing groups along with a possible formation of various small molecular compounds (N-rich) that are more stable thus much slower removed in the second period of 4 h.

The absorbance measurements on the mono- component samples (Fig. 11) show the characteristic UV absorption peaks for TiO_2 and SnO_2 and Vis absorption peaks for CuInS_2 . In multi-layered samples, the actual band gap values and their position might be slowly shifted due to the testing conditions and synthesis parameters. The overall absorbance remains similar with the sum of each spectral range of each layer. However, the charge carrier flow through the tandem structure is faster due to a higher absorbed energy compared with the tandem effective band gap [51].

Another advantage of the tandem structure is the simultaneous use of UV and Vis radiation that supports a synergetic effect of multiple charge carriers injection through the system at each junction. These results are in agreement with the energy bands diagrams and explain why the multi-component tandem structure has better photocatalytic properties. The addition of low effective band gap and high energy absorbance components supports the charge carriers generation and consequently the formation of oxidative species needed to mineralize the organic pollutants.

4. Conclusions

Tandem multi-layered thin films of SnO_2 , TiO_2 and CuInS_2 were prepared by RSPD followed by annealing. The samples have uniform morphology with grain sizes between 300 nm (SnO_2 , CuInS_2) and 700 nm (TiO_2). The components in the tandem systems have structural compatibility and similar crystallites' sizes.

The photocatalytic investigations in aqueous solutions confirm that the tandem systems have improved photocatalytic activity compared to the mono-component samples. The highest photocatalytic efficiency in the MB removal (92.3%) was obtained when using the three-component tandem $\text{CuInS}_2/\text{TiO}_2/\text{SnO}_2$. The long term tests showed that interim water-cleaning steps support the catalyst re-activation and allow obtaining, after 36 h high, TOC removal efficiencies higher than 90% when using the CIS_TO_SO sample. The (VB) and (VC) values of the components in the tandem are suitably positioned, supporting the charge carrier generation and mobility. Considering the absorption spectra, the tandem photocatalysts will generate charge carriers, both under UV and Vis irradiation. The photocatalytic activity in this tandem structure is explained by the higher absorbed energy compared with the effective band gap.

The surface energy outlines a hydrophilic behavior, which is beneficial for photocatalytic processes in aqueous solutions or humid media. The highest surface energy (138.3 mN/m) corresponds to samples where CuInS_2 is the top layer.

Long term runs proved the stability of the photocatalytic activity of the thin films after 36 h if an intermediate washing step is included after each 12 h, to remove the adsorbed by-products.

The combination of efficiency and stability makes these tandem thin films promising alternatives in up-scaled photocatalytic processes for advanced wastewater treatment. Additionally, the use of inorganic precursors and a common industrial deposition method (SPD) can support technology acceptance, in the general effort toward water re-use.

Acknowledgment

This work was performed through the partnerships in priority areas—PNII MEN_UEFISCDI project no. 282/2014.

References

- [1] F. Tisa, A.A. Raman, W.M. Daud, J. Environ. Manag. 146 (2014) 260–275.
- [2] M. Gong, Y. Li, H. Wang, Y. Liang, J.Z. Wu, J. Zhou, J. Wang, T. Regier, F. Wei, H. Dai, J. Am. Chem. Soc. 135 (2013) 8452–8455.
- [3] R. Homlok, E. Takács, L. Wojnárovits, Chemosphere 91 (2013) 383–389.
- [4] C.P. Huang, C. Dong, Z. Tang, Waste Manag. 13 (1993) 361–377.
- [5] L.J. Sebren, J.J. Devery, C.R.J. Stephenson, ACS Catal. 4 (2014) 703–716.
- [6] D. Błędzka, M. Gmurek, M. Grygliński, M. Olak, J.S. Miller, S. Ledakowicz, Catal. Today 151 (2010) 125–130.
- [7] Y. Liang, Y. Li, H. Wang, H. Dai, J. Am. Chem. Soc. 135 (2013) 2013–2036.
- [8] N. Serpone, S. Horikoshi, A.V. Emeline, J. Photochem. Photobiol. C 11 (2010) 114–131.
- [9] K. Nakata, A. Fujishima, J. Photochem. Photobiol. C 13 (2012) 169–189.
- [10] R. Morrish, T. Haak, C.A. Wolden, Chem. Mater. 26 (2014) 3986–3992.
- [11] A.M. Ali, A.A. Ismail, R. Najmy, A. Al-Hajry, J. Photochem. Photobiol. A 275 (2014) 37–46.
- [12] N. Talebian, F. Jafarizadeh, Ceram. Int. 39 (2013) 8311–8317.

- [13] J.M. Frost, K.T. Butler, F. Brivio, C.H. Hendon, M. Schilfgaarde, A. Walsh, *Nano Lett.* 14 (2014) 2584–2590.
- [14] M. Takeuchi, M. Hidaka, M. Anpo, J. Hazard. Mater. 237–238 (2012) 133–139.
- [15] Z. Mesgari, M. Gharagozlou, A. Khosravi, K. Gharanjig, *Appl. Catal. A-Gen.* 411–412 (2012) 139–145.
- [16] S. Chen, W. Zhao, W. Liu, S. Zhang, *Appl. Surf. Sci.* 255 (2008) 2478–2484.
- [17] C. Valentin, M. Rosa, G. Pacchioni, *J. Am. Chem. Soc.* 134 (2012) 14086–14098.
- [18] S.H. Hwang, C. Kim, J. Jang, *Catal. Commun.* 12 (2011) 1037–1041.
- [19] E. Thimsen, Q. Peng, A.B.F. Martinson, M.J. Pellin, J.W. Elam, *Chem. Mater.* 23 (2011) 4411–4413.
- [20] A. Pedone, G. Malavasi, M.C. Menziani, A.N. Cormack, U. Segre, *J. Phys. Chem. B* 110 (2006) 11780–11795.
- [21] A. Enesca, L. Isac, A. Duta, *Appl. Catal. B- Environ.* 162 (2015) 352–363.
- [22] A. Enesca, L. Isac, A. Duta, *Thin Solid Films* 542 (2013) 31–37.
- [23] A. Enesca, L. Andronic, A. Duta, *Catal. Lett.* 142 (2012) 224–230.
- [24] J. Yang, J. You, C.C. Chen, W.C. Hsu, H. Tan, X.W. Zhang, Z. Hong, Y. Yang, *ACS Nano* 5 (2011) 6210–6217.
- [25] A.K. Karnal, A. Saxena, S. Ganesamoorthy, I. Bhaumik, V.K. Wadhawan, H.L. Bhat, P.K. Gupta, *J. Cryst. Growth* 297 (2006) 152–156.
- [26] H.B.R. Lee, M.N. Mullings, X. Jiang, B.M. Clemens, S.F. Bent, *Chem. Mater.* 24 (2012) 4051–4059.
- [27] L. Sheng, W. Xuebin, N. Longying, C. Lijin, Y. Ru, *Thin Solid Films* 585 (2015) 72–75.
- [28] C.Q. Sun, *Prog. Solid State Chem.* 35 (2007) 1–159.
- [29] X. Chen, J. Pang, G. Zhou, B. Sun, *Colloid Surf. A* 481 (2015) 176–185.
- [30] T. Shen, X. Qi, R.B. Nellas, *J. Phys. Chem. B* 117 (2013) 12844–12849.
- [31] K. Mitsuhashi, N. Tagami, K. Tanabe, S. Suzuki, S. Iwanaga, T. Ohkubo, H. Sakai, M. Koishi, M. Abe, *J. Photochem. Photobiol. A* 185 (2007) 133–139.
- [32] S. Nishimoto, M. Becchaku, Y. Kameshima, Y. Shirosaki, S. Hayakawa, A. Osaka, M. Miyake, *Thin Solid Films* 558 (2014) 221–226.
- [33] G. Zhang, X. Zhang, M. Li, Z. Su, *ACS Appl. Mater. Interfaces* 6 (2014) 1729–1733.
- [34] J. Park, H.S. Han, Y.C. Kim, J.P. Ahn, M.R. Ok, K.E. Lee, J.W. Lee, P.R. Cha, H.K. Seok, H. Jeon, *Nat. Sci. Rep.* 5 (18150) (2015) 1–12.
- [35] D. Exerowa, N.V. Churaev, T. Kolarov, N.E. Esipova, N. Panchev, Z.M. Zorin, *Adv. Colloid Interfacace* 104 (2003) 1–24.
- [36] L. Isac, I. Popovici, A. Enesca, A. Duta, *Energy Procedia* 2 (2010) 71–78.
- [37] T. Mise, T. Nakada, *Thin Solid Films* 518 (2010) 5604–5609.
- [38] S.P. Gao, *Solid State Commun.* 152 (2012) 1817–1820.
- [39] A. Enesca, L. Isac, L. Andronic, D. Perniu, A. Duta, *Appl. Catal. B- Environ.* 147 (2014) 175–184.
- [40] D.O. Scanlon, C.W. Dunnill, J. Buckeridge, S.A. Shevlin, A.J. Logsdail, S.M. Woodley, C.R.A. Catlow, M.J. Powell, R.G. Palgrave, I.P. Parkin, G.W. Watson, T.W. Keal, P. Sherwood, A. Walsh, A.A. Sokol, *Nat. Mater.* 12 (2013) 798–801.
- [41] L.T. Kunneman, M.D. Tessier, H. Heuclin, B. Dubertret, Y.V. Aulin, F.C. Grozema, J.M. Schins, L.D.A. Siebbeles, *J. Phys. Chem. Lett.* 4 (2013) 3574–3578.
- [42] C.H. Yeh, Y.C. Lin, Y.C. Chen, C.C. Lu, Z. Liu, K. Suenaga, P.W. Chiu, *ACS Nano* 8 (2014) 6962–6969.
- [43] Y.B. Tang, L.C. Yin, Y. Yang, X.H. Bo, Y.L. Cao, H.E. Wang, W.J. Zhang, I. Bello, S.T. Lee, H.M. Cheng, C.S. Lee, *ACS Nano* 6 (2012) 1970–1978.
- [44] F. Karlický, M. Otyepka, *J. Chem. Theory Comput.* 9 (2013) 4155–4164.
- [45] P. Ju, P. Wang, B. Li, H. Fan, S. Ai, D. Zhang, Y. Wang, *Chem. Eng. J.* 236 (2014) 430–437.
- [46] C. Karunakaran, P. Vinayagamoorthy, J. Jayabharathi, *Langmuir* 30 (2014) 15031–15039.
- [47] Y. Lin, Z. Jiang, R. Zhang, C. Zhu, X. Hu, X. Zhang, H. Zhu, *J. Catal.* 309 (2014) 115–120.
- [48] S. Liu, X. Chen, *J. Hazard. Mater.* 152 (2008) 48–55.
- [49] T. Nonoyama, T. Kinoshita, M. Higuchi, K. Nagata, M. Tanaka, K. Sato, K. Kato, *J. Am. Chem. Soc.* 134 (2012) 8841–8847.
- [50] B. Li, Y. Dong, C. Zou, Y. Xu, *Ind. Eng. Chem. Res.* 53 (2014) 4199–4206.
- [51] S.C. Wang, M.Y. Lu, A. Manekkathodi, P.H. Liu, H.C. Lin, W.S. Li, T.C. Hou, S. Gwo, L.J. Chen, *Nano Lett.* 14 (2014) 3241–3246.